

Supplement of Atmos. Chem. Phys., 19, 8999–9015, 2019
<https://doi.org/10.5194/acp-19-8999-2019-supplement>
© Author(s) 2019. This work is distributed under
the Creative Commons Attribution 4.0 License.



Supplement of

H₂SO₄ and particle production in a photolytic flow reactor: chemical modeling, cluster thermodynamics and contamination issues

David R. Hanson et al.

Correspondence to: David R. Hanson (hansondr@augzburg.edu)

The copyright of individual parts of the supplement might differ from the CC BY 4.0 License.

Supplement.

S1.0 Typical raw data and analysis.

Shown in the figure below are raw counts for the ten channels (i.e., voltages sent to the nanoDMA) that are routinely monitored in all experiments. The data from 12:00 to 13:20 is for $Q_4 = 5.3$ sccm (red line is Q_4) and many channels show a variability of 20-to-50 % over a 80 min time period. At the lowest voltages and thus smallest particle sizes, random fluctuations due to counting statistics are apparent (each data point has a collection time of 10 s.) In table S1 are the actual voltages sent to the nanoDMA, the corresponding mobility diameters, and the overall correction factors. Note the large increases in count rates at 13:20 due to introduction of ammonia. Although there is some drift and the average of the data from 13:28 to 13:44 was flagged, the channels settle to a somewhat steady level by about 13:30. Later, the count rates at the lower HONO settings (red line) were steady and the averages were deemed valid data points.

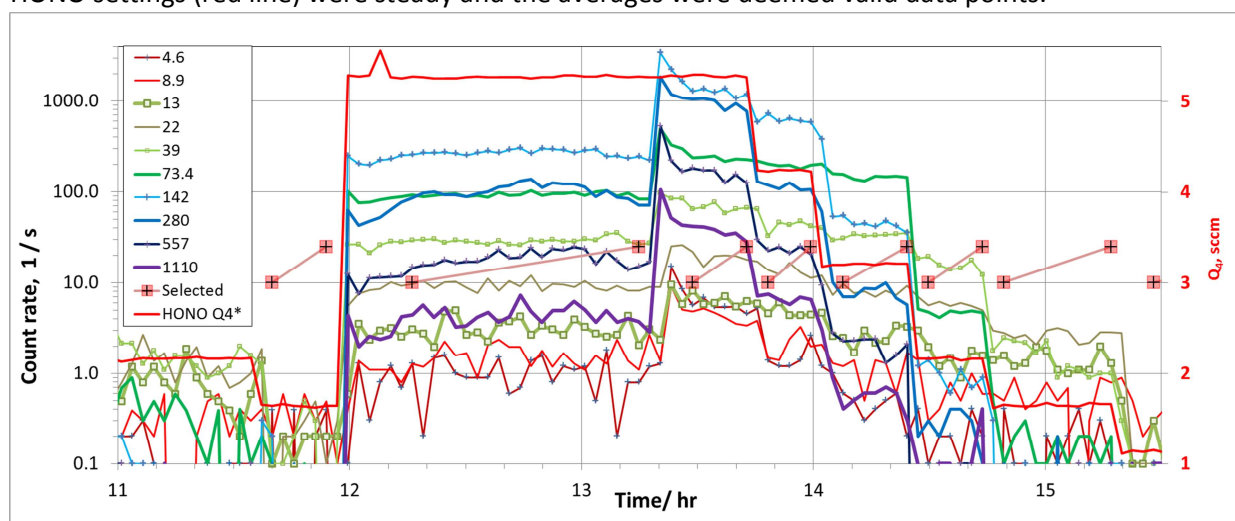


Fig. S1. CPC Raw count rates vs. time for the channels (i.e. particle sizes) monitored with the DEG system. Each channel's set voltage for the nanoDMA's high-voltage source are indicated in the figure: due to electrical offsets, the voltages applied were actually 2 V higher (see Table S1). The thick red line is the flow rate of the HONO mixture and the pink squares joined by slanted lines mark each time-selected range of data for averaging to yield a size distribution. At 13:20, ammonia at 440 pptv was added at the top of PhoFR (2018Jun13).

Table S1. Voltage on the nanoDMA center rod, mobility diameter, and the overall correction factor for particle losses, charging efficiency etc. (Jiang et al. 2011.)

actual V	mob. diam. (nm)	Corrections
6.6	1.70	6830
10.9	2.19	1500
15	2.57	733
24	3.26	323
41	4.27	150
75	5.80	72
144	8.02	38
282	11.25	22
559	15.87	13.6
1112	22.43	9.1

S1.1 Leading edge of the size distributions

The leading edge mode of the size distributions were fit to log-normal functions using an Excel add-in (written in Visual Basic, "LgnFit.xlam", M. R. Stolzenburg, private communication). The routine 'LgnFit' fits a log-normal to the upper portion of a measured distribution, resulting in leading-edge parameters D_{le} , $\ln\sigma_{le}$ and $N_{p,le}$. Shown in Fig. S2 are a typical measured distribution and two lognormals, one using LgnFit and one that was manually fit to the leading edge particles. The fitting routine included the 4.3 nm data and thus resulted in a wider distribution. Which of the two lognormals is best for interpreting the data may depend on what physical process is being probed. In terms of the size to which the largest particles can grow, the mode diameters of these lognormals are not significantly different.

We have identified a "leading edge" of the size distribution which is "leading" in terms of particle growth. This "leading edge" terminology refers to the large-particles at the leading edge of the distribution and here we clarify this further. This is beyond what one would naturally think of as the leading edge particularly as we fit lognormals to this data which requires to some extent data on both sides of a peak. So if the large particle peak is prominent, data for the fit should extend from the "leading edge" at the far right all the way down in size to an inflection point between the large particle peak and the minimum towards smaller sizes. Note that N_p is for "large particles" that are defined differently: all those with $D_p \geq 2.4$ nm. It is important to maintain the distinction of which criterion was used to derive any particular parameter (e.g. D_{le} , not D_p). In practice, the integration of the lognormal fit and N_p do not differ appreciably.

Some distributions without base added do not exhibit a prominent large particle peak. In these cases either no or an inappropriate inflection point was selected. When no inflection point is exhibited, they were not able to be fit automatically. These cases were not included in the D_{le} plots but we note that lognormals fitted by eye, using an average width from contemporary distributions, yield D_{le} values that fall within the scatter of the expected values. Some distributions yielded automatic fits that exhibited widths that were very large because the inflection point was too low in diameter. In these cases, the routine was forced to ignore one or two of the smallest diameter data points. A width criteria was used in these cases: the smallest diameter data were excluded one at a time until $\ln\sigma \leq 0.4$ for $Q_4 \leq 4.3$ sccm and $\ln\sigma \leq 0.55$ at higher Q_4 . Fig. S2 below for a $Q_4 = 4.3$ sccm distribution is one such case. For this data set, the inflection point criteria in the automatic fitting routine also included the next smallest diameter data point and resulted in a $\ln\sigma = 0.5$.

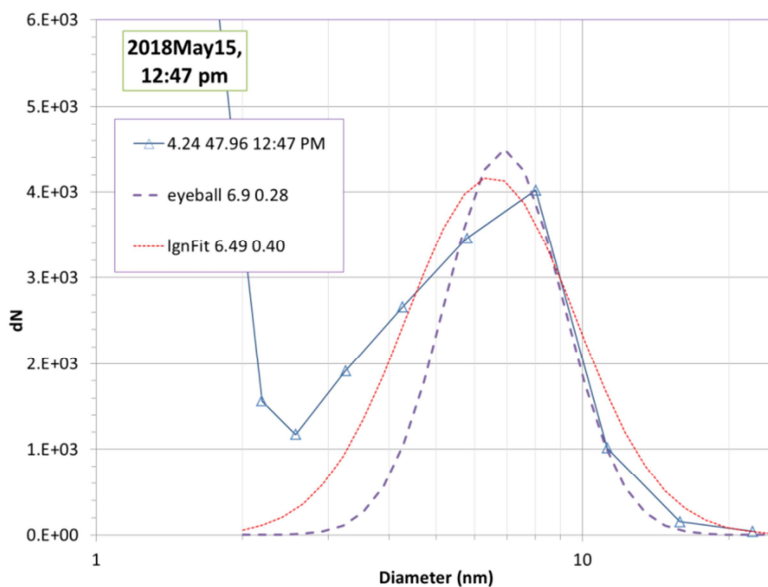


Fig. S1.1. Measured size distribution and two log-normals: one manually fit (eyeball) and the other using a fitting routine (lgnFit). The mode diameter and $\ln\sigma$ are indicated in the figure. The vertical axis is corrected concentration. Including the data point at 3.3 nm brings in smaller particles that probably did not originate in the top 1/3 of the flow reactor.

S1.2 Typical measured size distributions.

Depicted in Figs. S1.2.1 are representative particle size distributions as a function of N_2 flow through the HONO source, Q_4 , a proxy for HONO abundance. Q_4 was varied from 1.6 to 5.3 sccm while the abundances of the other reactants were held constant. The size distributions are strongly dependent on HONO over this range, with concentrations increasing by a factor of \sim ten at small sizes and the large particle abundance by a hundred-fold. Log-normal distributions are also shown as the dashed lines in the figure with leading-edge mode diameter $D_{l.e}$ and $\ln\sigma$ noted in the legend. The log-normals shown in the figure were not those from the fitting procedure (see S1.1 for a discussion of the fitting procedure) because the fits failed for the two lowest Q_4 . For a consistent presentation, $\ln\sigma$ was fixed and each log-normal was adjusted visually to best cover the four or five points nearest the peak of each distribution. Note that raw count rates at the smallest size for the three lowest Q_4 are roughly 0.1 s^{-1} and, statistically, they are not significantly different. This is slightly above the background count rate of $\sim 0.05 \text{ s}^{-1}$.

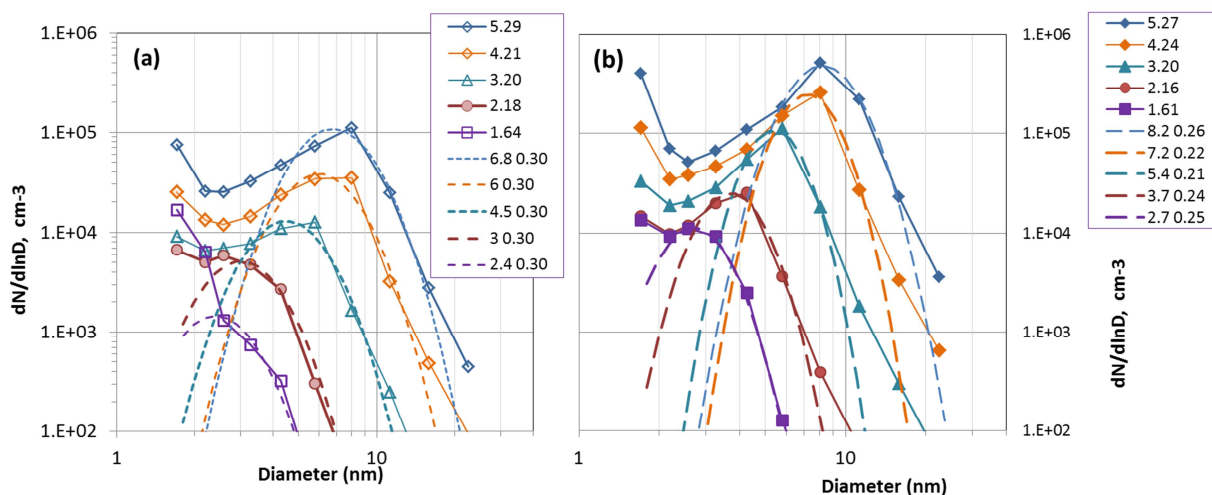


Fig. S1.2.1 Measured size distributions as a function of Q_4 , the flow rate through the HONO generator. Log-normal distributions fitted to the leading edge are shown as the dashed lines. Particle size distributions with (a) no added base and (b) with 230 pptv NH_3 present. The data (solid lines with symbols) have Q_4 /sccm listed in the legends. The log-normal distributions (dashed lines) have mode diameter (nm) and $\ln\sigma$ listed in sequence in the legends.

The volume mean diameters from nearly all of the measured nominally-binary size distributions are plotted vs. Q_4 in Fig. S1.2.2(a-c). Panel (a) shows $D_{V,l.e.}$ as a function of Q_4 , panel (b) is $D_{V,l.e.}$ vs. relative humidity and (c) is $D_{V,l.e.}$ as a function of SO_2 abundance. Not all experiments yielded leading-edge log-normal fits; these were primarily for Q_4 values less than or equal to 2.2 sccm in (a).

The data is linear in plot (a) over the range 2.2 to 8.5 sccm in Fig. S1.2.2(a) and a linear fit is shown as the line. The largest Q_4 data points fall a little below the line and perhaps the distribution of H_2SO_4 is significantly perturbed by the large particle surface area, decreasing the connection between Q_4 and growth. Plot (b) also shows a linear relationship between size and relative humidity, a phenomenological finding that has a slightly higher RH dependency than a simple swelling of the particles due to uptake of water vapor (see the solid line). Plot (c) shows the experimental and growth-rate calculated diameter as a function of SO_2 .

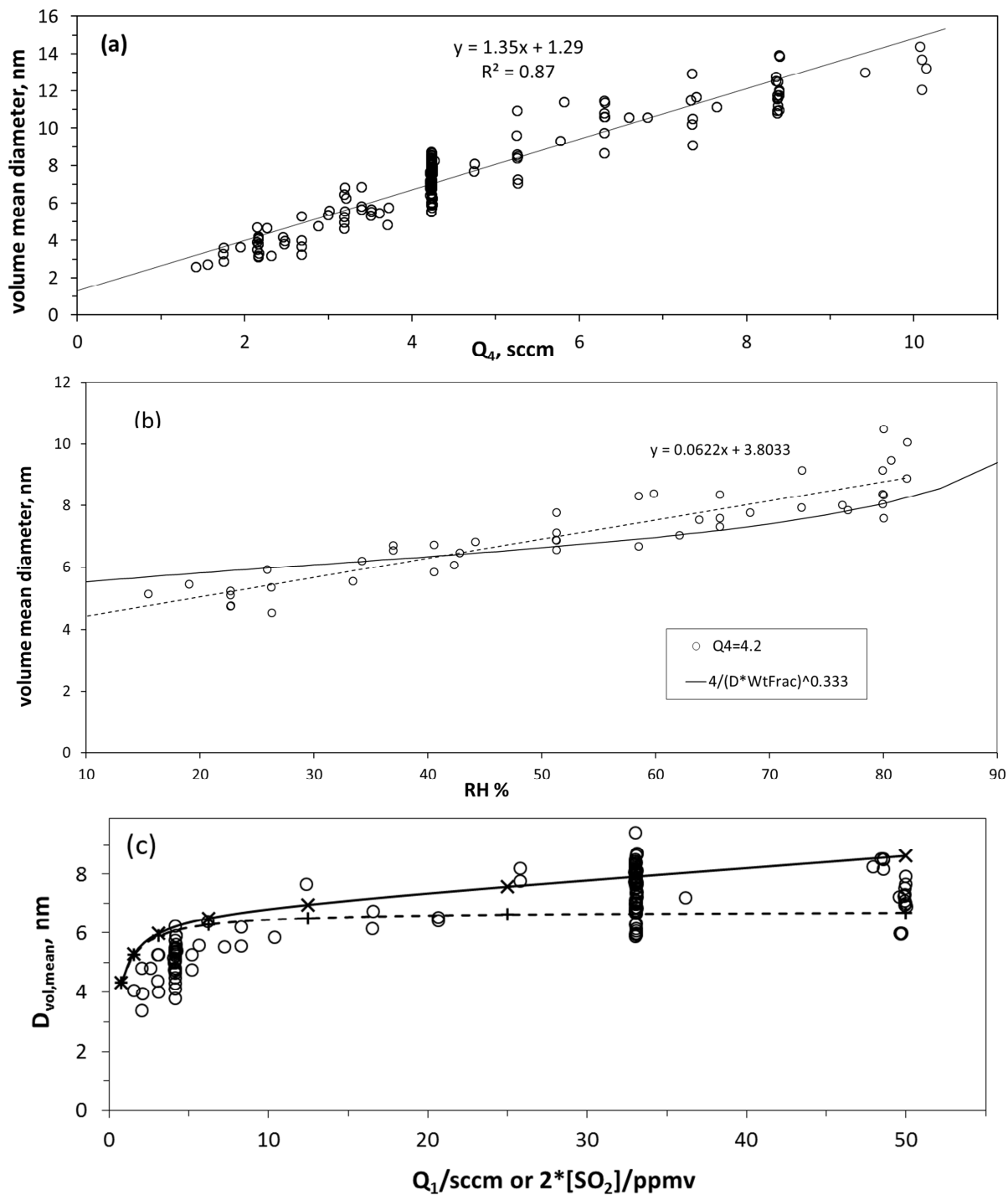


Fig. S1.2.2. Volume mean diameter of the particles in the leading edge of the particle distributions, $D_{V,le} = D_{le} \cdot \exp(1.5 \ln \sigma^2)$. Top plot (a) $D_{V,le}$ vs. Q_4 at 52 % RH. Data from those distributions that had a local minimum between the smallest particles and the peak at large diameters that allowed for fit. (b) $D_{V,le}$ vs. RH at $Q_4 = 4.2$ sccm. A linear fit is shown as the dashed line (phenomenological) while the solid line is the diameter increase based on water uptake using bulk values for the density and mass fraction of H_2SO_4 as a function of RH (Wexler and Clegg, 2002). (c) $D_{V,le}$ vs. Q_1 , the flow rate of the SO_2 mixture for 52 % RH and $Q_4 = 4.2$ sccm. The dashed and solid lines are diameters derived from simulated growth rates without and with, respectively, a reaction included for HO_2 with SO_2 . The size was estimated from the H_2SO_4 growth rate and particle transit time assuming particles nucleate at 1 nm mass diameter. Also applied was the mobility to mass size difference of 0.3 nm (Larriba et al.)

Finally, size distributions for $Q_4 = 4.2$ sccm and $Q_1 > 16$ sccm for the bulk of the measurement period are shown in Fig. S1.2.3. The scatter in the measurements is clearly the dominant feature in these plots. Yet in an overall sense, it appears that particles taken in the latter time period are somewhat less abundant. However, any differences are obscured by the overlap of the scatter in the individual distributions.

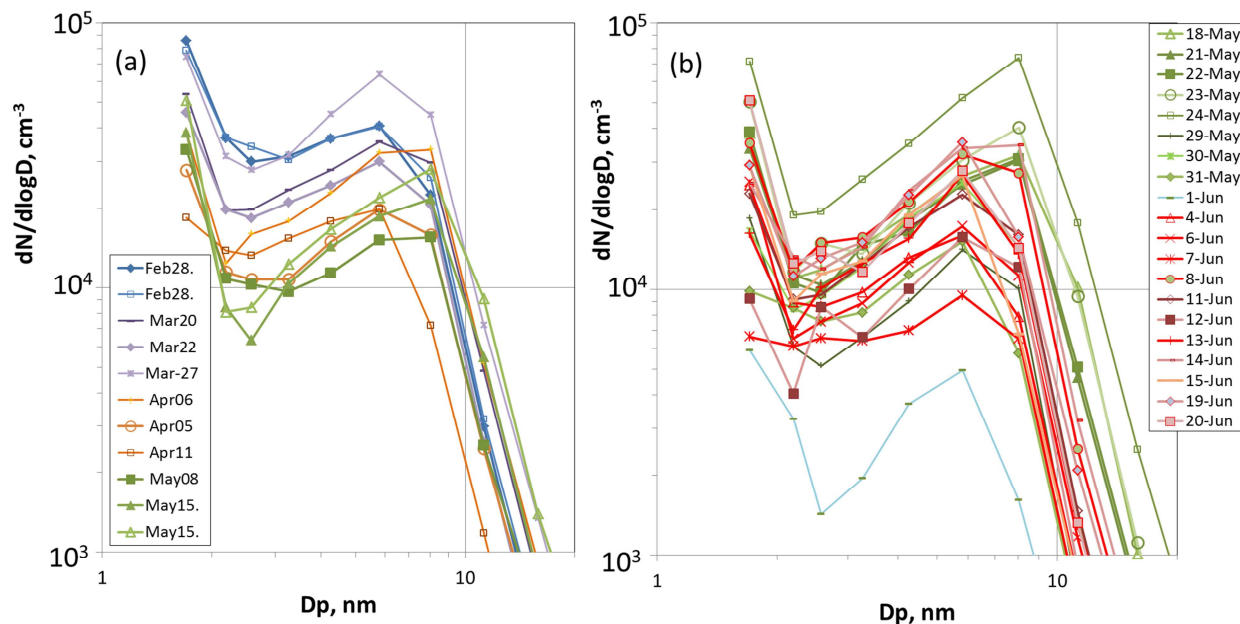


Fig. S1.2.3. Measured size distributions from late February, 2018 to mid-May (left plot) and mid-May to late June (right plot). Experimental conditions: $Q_1 > 32$ sccm, $Q_4 = 4.2$ sccm, nominally pure.

S1.3 Modeled size distributions.

Shown in Fig. S1.3.1a,b,c below are typical model results for nucleation due to only the binary system (a) as incorporated for 52 % RH, and nucleation with 200 pptv NH_3 added (b) using a new set of $\text{NH}_3\text{-H}_2\text{SO}_4$ thermodynamics, scheme $\text{NH}_3\text{-52}$ (aka B52#ZtriplePrime). These thermodynamics are presented in S8 below. The development of the size distributions are illustrated in a series of distributions at different lengths down the flow reactor for a HONO source flow of $Q_4 = 2.1$ sccm. Clusters up to 250 H_2SO_4 molecules were simulated. Panel c shows the size distributions at $Z = 120$ cm where particles are sampled for the binary and added ammonia cases from a and b as well as a size distribution for 0.005 pptv added dimethylamine. Shown in Fig. S1.3.2 are the $R = 0$ concentrations vs. axial distance of a few select clusters for the simulation shown in Fig. S1.3.1b.

The characteristics of the distributions change in expected ways along the length of the flow reactor. The binary system results (Fig. S1.3.1a) have N_p increase dramatically with distance along the flow reactor (N_p/cm^{-3} is the second column in the legend; N_p is the sum of all particles with mobility diameters $D_p > 2$ nm which are cluster sizes > 10 H_2SO_4 molecules), while N_p in the added NH_3 case is relatively constant in the lower half of the reactor. From 80 to 120 cm, the number of large particles increases by a factor of 20 in the binary case while in the added NH_3 case this number increases by a factor of only 1.4. The “large particles” in general grow larger as they flow down the reactor with this growth best exhibited in the added- NH_3 case with a nice progression in the peak towards large sizes in the distributions from 60 to 120 cm.

Comparing the simulated 120 cm distributions with and without added base (Fig.S1.3.1c where additional simulations where 0.005 and 2 pptv dimethylamine were included) illustrates how the size distributions form.

The smallest clusters of $D_p < 1.8$ nm have high concentrations in all cases at the end of the reactor because of the peak in H_2SO_4 in that region. The large particle mode is apparent in all cases as well but the shapes and abundances are different. In the case of added NH_3 , the large particle mode is indicated by a strong leading edge with a peak at 4 nm while the binary only size distribution is smaller with a shallow peak at 2.6 nm. Ammonia's influence is large for large particles, those that nucleate near the top of PhoFR but the mid-sized particle numbers are also significantly increased. Despite its rapid diffusion and loss on the wall, enough ammonia makes it far enough into the reactor to affect the mid-sized particles: the model (Fig. S1.3.2) shows that about 10 % of the initial $[NH_3]$ is present on axis, halfway down the tube. The 5 ppqv dimethylamine simulation shows that this slower diffusing base species, which will be true for any amine or amide compared to ammonia, can have a relatively large impact on the mid-sized particles. The interplay between the effects on the size distributions depends on what type of impurity is present and where it originates. There is excellent agreement between simulated and experimental for the 2 pptv dimethylamine-added case except towards large particles.

Even though the shapes of the distributions compare favorably with experiment for nominally clean and for added NH_3 , the disparity in the total number of particles indicates there is some deficiency in the phenomenological thermodynamics for these conditions. Yet this could also be due to a contaminant that is more nucleation-active than ammonia such as an amine (Glasoe et al.) and thus it could have an influence even if present at very low levels. The thermodynamics used here (see S8) are phenomenological and set by comparison with the high ammonia data for $Q_4 = 4.2$ sccm. This was done because under these conditions nucleation will be less influenced by any potential contaminant. So the under-prediction of the simulations at $Q_4 = 2.1$ sccm may not be a flaw in the thermodynamics but probably indicates a larger sensitivity to contaminant at the lower sulfuric acid conditions.

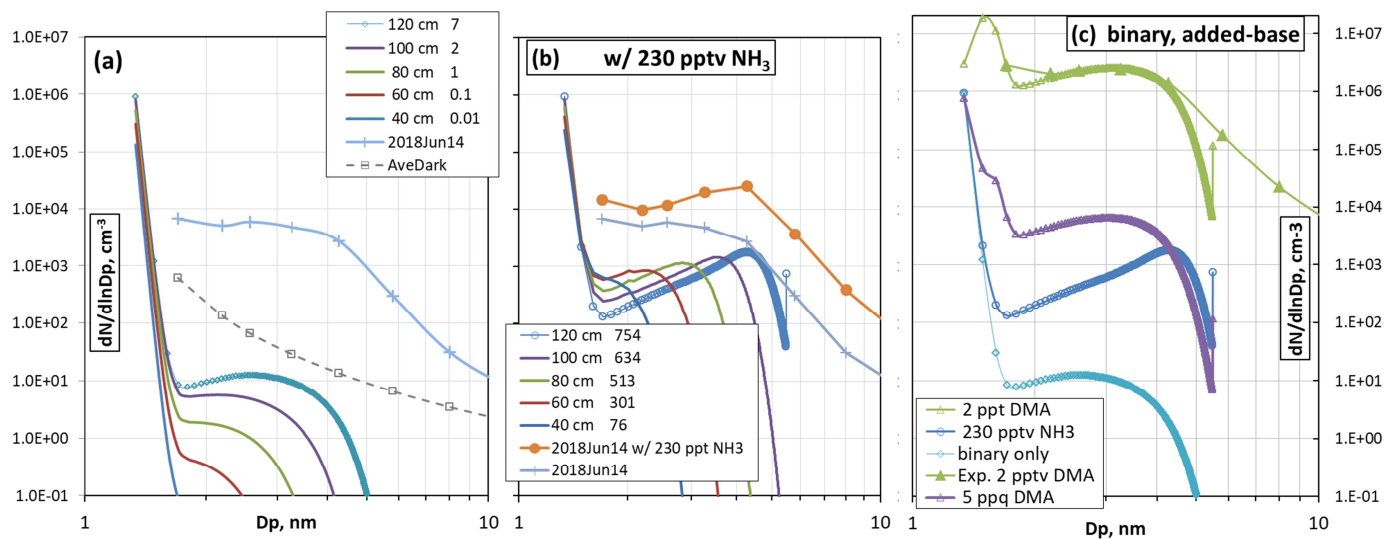


Fig. S1.3.1. Centerline size distributions for $Q_4=2.1$ sccm, experiment and simulations. Simulated clusters from 2 to 250 sulfuric acid molecules (summed over base-content) shown at 5 axial positions along the flow reactor: (a) Binary simulations and (b) 200 pptv NH_3 added simulations. Measured size distributions are for the nominally binary case and for 230 pptv NH_3 added (a typical dark count 'distribution' is also shown in a). (c) Simulated size distributions at 120 cm for the binary, 200 pptv NH_3 and 0.005 pptv dimethylamine-added. Experimental (see Figs. 4a and S3.2(a)) and simulated 2 pptv dimethylamine-added also shown.

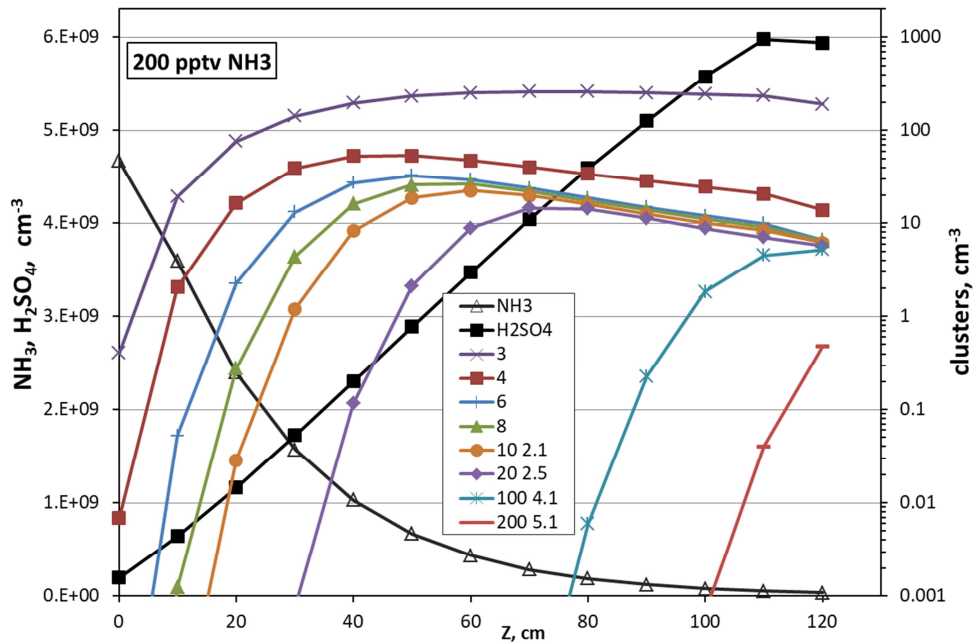


Fig. S1.3.2. Axial concentrations for the simulation of Fig S1.3.1b. Ammonia and sulfuric acid axial concentrations on the left axis and plotted on the right axis (log-scale) are the $a_{3,4,6,8,10}b_x$ clusters (labeled 3 4 6 8 10 in the legend) - concentrations were the sum over x, and three growth-only clusters (labeled by # of sulfuric acid molecules and mobility diameter in nm).

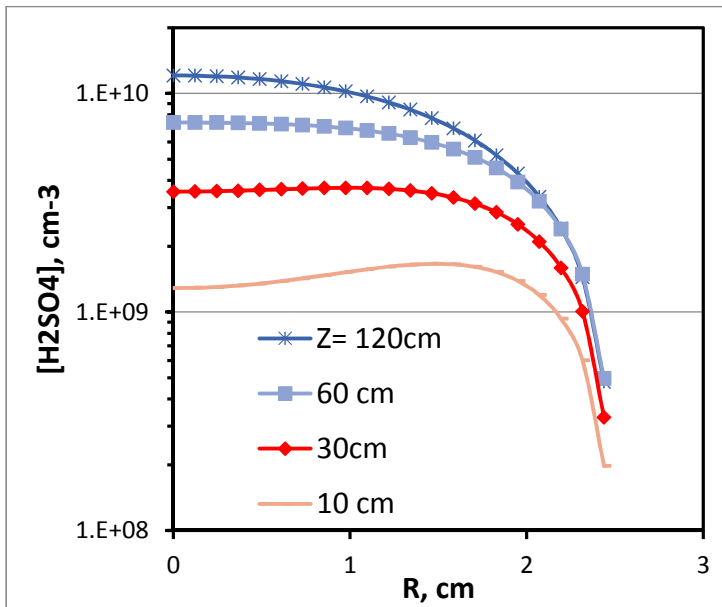


Fig. S1.3.3. Radial profiles for sulfuric acid at four positions along the flow reactor. Simulated baseline conditions: $Q_4=4.2$ sccm, $Q_1=32$ sccm.

S2. Historical PhoFR data

During the course of this study, the experimental apparatus was moved to a lab in a newly-constructed building. The gas source was switched from cleaned air (AADC0 737) to nitrogen from a liquid nitrogen gas-pack dewar (Airgas). This nitrogen is listed as having < 10 ppm oxygen impurity level, and apparently there is enough present as there was little effect on size distributions when oxygen was added. Data for typical baseline conditions for the year previous to this move are presented in Fig. S2.

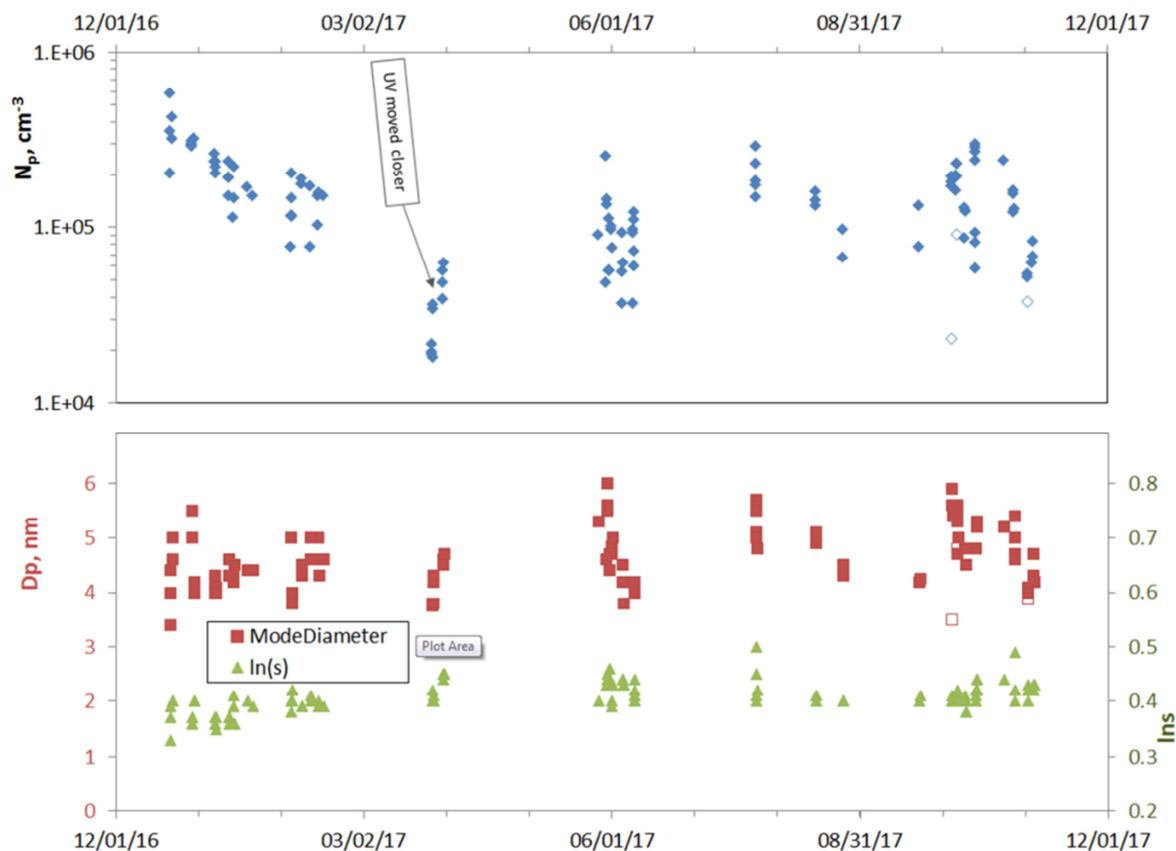


Figure S2(a,b) Data for typical conditions: 50 % RH, 296 K, total flow of 3 sLpm, $Q_4=4.3$ sccm and $Q_{\text{SO}_2\text{mix}}=4.1$ sccm (the latter two result in HONO of 20 ppbv and $\text{SO}_2 = 2$ ppmv). (a) Total particle number density, N_p , and (b) the mode diameter and $\ln\sigma$ as a function of time (from manually-fitted/eyeball lognormals). Although at higher SO_2 levels, $Q_1=32$ sccm, the size distributions shown in Fig. S1.2.3 reveal a similar scatter in D_p and total particle number concentration as depicted in S2.

Over this time period, N_p averages about $1 \times 10^5 \text{ cm}^{-3}$, the mode diameter has an average of about 5 nm, and the majority of the $\ln\sigma$ values are between 0.4 and 0.44. Since late March 2017, when the UV lights were moved a few cm closer to the flow reactor, trends in the data with time are not evident although the scatter remains significant. Three recent data points are not filled in and they were taken just before the NaONO(s) powder was lightly shaken. It is noteworthy that this process makes a difference however the effect is variable, e.g. in early November 2017 the NaONO vessel was shaken and the N_p increase was only about 25 %, less than the +100 %/-50 % day-to-day variability. The causes of this variability have not been identified but temperature variations are a likely cause, that of the room as well as that of the HCl-source.

S3. Experiments with added base: sizes and distributions.

S3.1 NH_3

When NH_3 is added to PhoFR, the leading-edge particles of the size distributions become very well-defined. This is also true for the measurements presented in Glasoe et al. (2015), but in that case the very low number of particles without the dilution system attached, less than 1 cm^{-3} , indicated a very clean flow reactor. The probable contaminant amine in the ammonia dilution system used by Glasoe et al. is a separate issue.

Shown in Fig. S3.1 are representative size distributions for the present measurements taken in PhoFR (2018Jun13) and for measurements in the Nucleation Flow Reactor (NFR) used by Glasoe et al. (2013Jun27)

along with a more recent measurement from that apparatus (2016_01_20). The size distribution from January 2016 is very narrow compared to the others and this is probably due to the 25 °C temperature of the mixing region and sulfuric acid reservoir (these were regulated at 35 °C for the Glasoe et al. data set.) Very important to keep in mind is that the abundance of H_2SO_4 in NFR is much different than it is in PhoFR: it is greatest near the top of NFR and drops by 2/3 or so as the particles travel to the DEG system. There are fewer particles in the present measurements but they are able to grow to larger sizes due to their larger overall exposure to H_2SO_4 in PhoFR. The size distribution from 2013 from Glasoe et al. is larger and broader than the others.

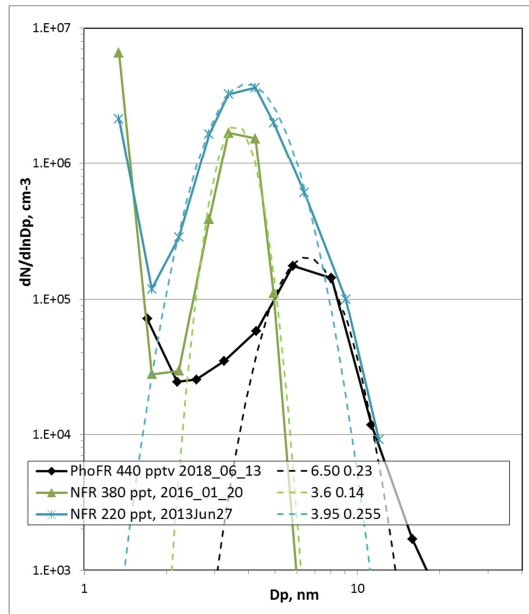


Fig. S3.1.1. Size distributions measured in PhoFR in comparison to those measured in NFR. NFR is the bulk-source flow reactor of Glasoe et al. 2015 with flows set such that $[\text{H}_2\text{SO}_4]$ is about $4 \times 10^9 \text{ cm}^{-3}$ where particles form. The 220 pptv NH_3 data is from Glasoe et al. while the 2016 data with 380 pptv NH_3 was taken with the bulk source held at a lower temperature (25 C vs. 35 C for Glasoe et al.) PhoFR data at 440 pptv with $Q_4=4.2 \text{ sccm}$ which is an $[\text{H}_2\text{SO}_4]$ estimated to be $3 \times 10^9 \text{ cm}^{-3}$ where nucleation occurs.

When NH_3 was added to PhoFR, lognormals from both the eyeball and LgnFit were affected. The leading-edge diameters increased and the widths decreased upon NH_3 addition. The change in diameter with added ammonia is demonstrated in Fig. S3.1.2, plots of mode diameters vs. HONO level (Q_4) for two different amounts of added NH_3 .

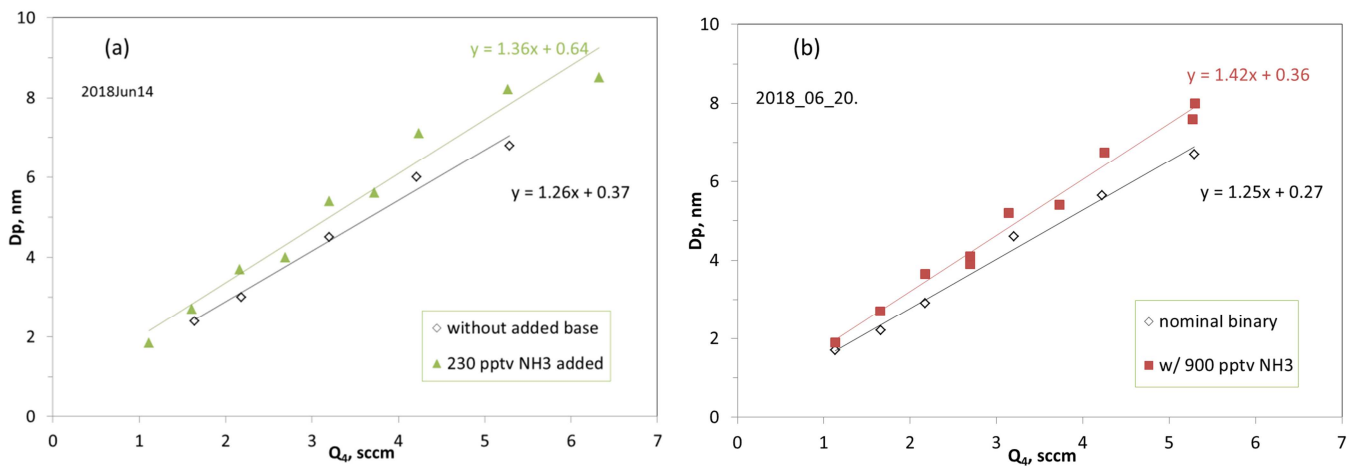


Fig. S3.1.2. D_p vs. Q_4 . Added ammonia (a) 230 pptv and (b) 900 pptv. Also shown as the diamonds are data for the nominally binary cases. $Q_1=33 \text{ sccm}$.

Bases are added from the dilution systems through a sidearm port at the top of PhoFR, about 10 cm below the Teflon mesh. We have used a similar system for base introduction where the tip of the exit tubing of the dilution system (of 1/8" OD) is installed so that it is flush with the flow reactor wall (Zollner et al., Ball et al., Glasoe et al.) and we found that a net flow of about 50 sccm through this tubing gave maximum particle number densities. In a later publication, (Hanson et al. 2017) we presented experimental and computational fluid

dynamics results that showed that a flow of 50 sccm (computational) and 60 sccm (experimental) carrier gas (nitrogen) resulted in a maximum in the number of particles.

Depicted in Fig. S3.1.3 are experimental results for 300 pptv NH_3 added to PhoFR at standard conditions. It shows that a flow of 35 sccm entering PhoFR from the dilution system gives a peak in the experimental particle

number. This is somewhat lower than for our previous experimental work but this is expected as the total flow rate here is 2900 sccm compared to 6000 sccm in that previous work (both flow reactors have 5 cm ID.) Further discussion of base mixing into the main flow is presented in S7.1.

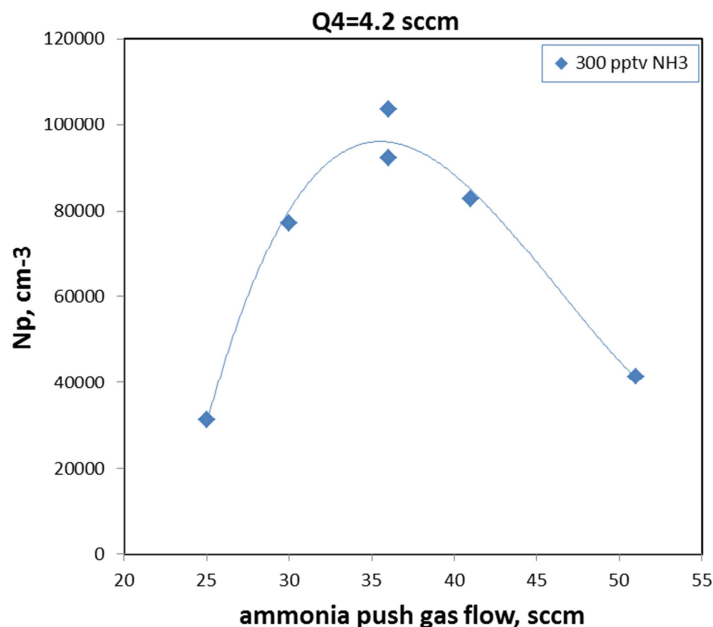


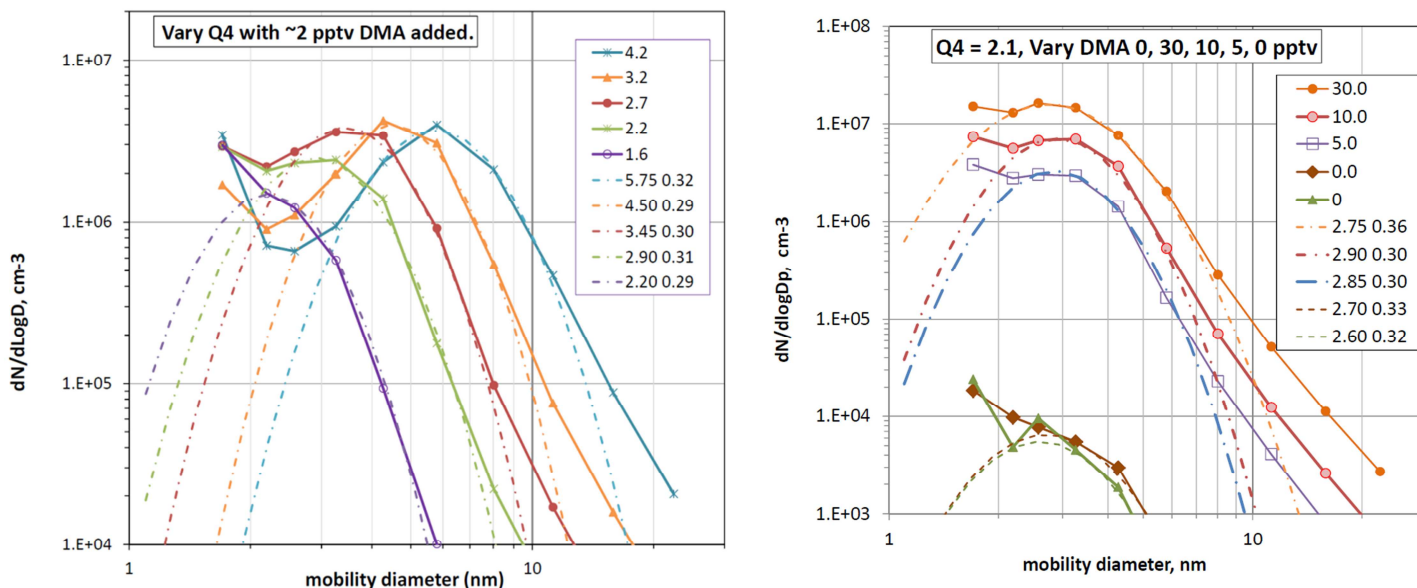
Fig. S3.1.3. Number of particles vs. net flow exiting the single dilution system to attain 300 pptv NH_3 . $Q_4=4.2$ sccm.

S3.2. Size distributions when dimethylamine was added.

The size distributions for the dimethylamine data presented in Figs. 4a and 5 are shown in Fig. S3.2 a and b. The zero-added base data between these runs might be affected by dimethylamine holdover but this appears to be small: the N_p are within a factor of two of the $Q_4=2.1$ sccm data in Fig. 4a. It is clear that more dimethylamine leads to more particles, with N_p increasing approximately linearly with dimethylamine abundance.

Particle-particle interactions at large N_p may act to weaken the connection between N_p and the actual nucleation rate which may contribute to the low dependence of N_p on Q_4 in Fig. 4a. Changes in dimethylamine concentrations due to scavenging by particles may also constrain the nucleation rate at the higher Q_4 conditions.

Fig. S3.2. Size distributions as a function of (a) Q_4 /sccm, HONO level, with 2 pptv dimethylamine added and (b) added dimethylamine at $Q_4 = 2.1$ sccm. The data in (a) were used in Fig. 4a and (b) were used in Fig. 5. In the legends, the entries with data points indicate Q_4 /sccm (a) and DMA/pptv (b), and the dash-dot labels indicate D_p and $\ln\sigma$.



S4. Dark Counts and Uncertainties.

At least daily, the UV lights were turned off to get a measure of the average dark counts. The count rate for these conditions was typically 0.05 s^{-1} but ranged as low as 0.02 s^{-1} and it was independent of reactant concentrations. Note that corrections for losses and charging efficiency increase as particles get smaller, thus there is an increase in corrected dark counts towards smaller particles. They can significantly influence the fits at the lowest Q_4 values, 2.2 sccm and lower, introducing additional uncertainty in the log-normal fit parameters.

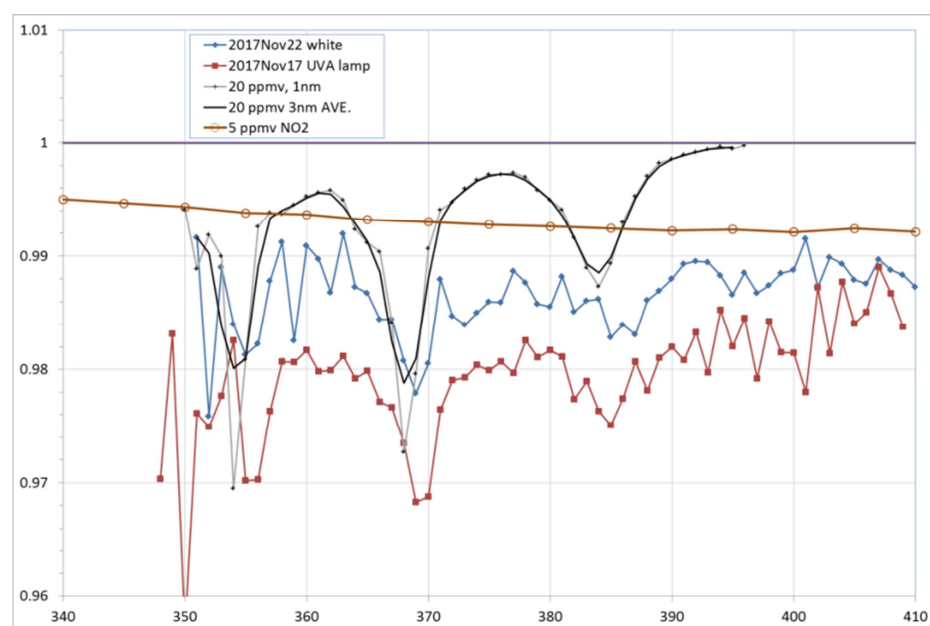
Having said that, we note that the smallest particles are not included in the $Q_4 = 4.2$ sccm data thus counting statistics are not a major contributing factor to the scatter evident in Figs. 2a, S3 and S4(a). The fitting procedure for some distributions can sometimes yield a range of log-normals that fit the data equally well however values for N_p and D_{le} are not sensitive to the choice of the log-normal. It is difficult-to-pin-down variations in the system that can be responsible for the scatter. As alluded to in S2, we believe the most likely causes are: (i) small temperature fluctuations in the HCl solution for the HONO source and (ii) inadvertent eddies or changes in the flow profile at the top of PhoFR. These may also introduce a bias in addition to scatter (thus a true systematic uncertainty) that may depend on trends in the temperature of the room. Usually, the temperature of the room was between 22 and 24 C but occasionally it was as warm as 26 C. If these temperature excursions also introduce a secular bias in flow patterns (which may have important implications for the modeling effort, see S7.2) is not known.

Large jumps in N_p and D_{le} could be due to episodic exposure of the flow reactor to room air and/or to dust, especially upon cylinder changeover. One such episode is depicted in Fig. 2a.

S5. Assessment of HONO level and photolysis rate.

S5.1 UV-Vis absorption experiment.

The HONO-containing flow was sent through a 1.05 m long absorption cell to assess the HONO level by absorption using a small diode array detector (Red Tide, Ocean Optics, ~ 3 nm resolution). The source was either a small UVA lamp or a white light. Shown in the figure are the transmissions for several measurements and the expected transmission for a HONO level of 20 ppmv (cross section from NASA data panel averaged over 4 nm). The absorptions for the two sources differ perhaps due to differences in scattered light within the instrument. There is a noticeable absorption at 400 nm and longer which can probably be assigned to NO₂ (see absorption due to 5 ppmv in Fig S5.1, NASA-15 cross sections). Syomin and Finlayson-Pitts (2003) saw HONO decay of about 10 % in a 100 min in the presence of 50 % RH. The water content of gas flowing from the HONO source is about 76% RH at 20 C which may decrease to about 50 % at 23-25 C, the temperature of the



absorption cell. Some loss of HONO and formation of NO₂ is expected but it is difficult to quantify to what extent from the previous work. It is also difficult to determine where this conversion may have happened.

Fig. S5.1. Measured absorption spectra of the flow exiting the HONO generation system. Representative transmission spectra for 20 ppm HONO (averaged over 1 nm and over 3 nm) and 5 ppmv NO₂ are also shown.

S5.2 PTRMS measurements of isoprene oxidation due to HONO photolysis.

The amount of OH-photolyte generated for typical conditions ($Q_4=4.3$ sccm, 3 sLpm total flow) was evaluated by adding isoprene to the flow and monitoring the amount of product methylvinyl ketone (MVK) and methacrolein (macr) using a PTRMS system (Hanson et al. 2009). An aliquot of isoprene in a diffusion tube, immersed in ice was teed into a flow entering PhoFR resulted in a level of isoprene = 6×10^{12} cm⁻³ as determined with a sensitivity of $S_{isop.} = 78$ ncps (aka Hz/ppbv/MHz) using isotopic ratio and the signal on mass 70: the $M.H^+$ signal at 69 u exceeded the linear range of the detector. This value of $S_{isop.}$ was the average of three values, determined from recent calibrations of the PTRMS for methanol, acetone and 3-pentanone and scaling them according to the ratios of sensitivities for isoprene to these compounds reported in Hanson et al. (2009). An increase in the signal at 71 u ($M.H^+$ for MVK + macr) of $\Delta S_{71u} = 2800$ Hz was observed when the UV lights were turned on (see left plot of Fig. S5.2). Assuming enough NO was present, a yield of 70% for these species is applicable (Liu et al., 2013; Wennberg et al., 2018) and assuming reaction with OH is negligible, the average production rate of MVK + macr (in cm⁻³ s⁻¹) in the illuminated portion of PhoFR is given by

$$\frac{d([MVK]+[macr])}{dt} = 0.7k_{OH+isop.}[OH][isop.]$$

which, assuming [OH] is uniformly produced, when integrated along the flow reactor gives

$$\Delta([MVK] + [macr]) = 0.7k_{OH+isop.}[OH][isop.]\tau_{res} \quad (\text{eq5.1})$$

where τ_{res} is the average residence time in the reactor. The [MVK] + [macr] determined from the PTRMS signals is given by

$$\Delta([MVK] + [macr]) = \frac{\Delta S_{71u}}{1.6S_{isop.}(S_0/1MHz)} 2.4 \times 10^{10} \quad (\text{eq5.2})$$

where the last term converts ppbv to cm^{-3} , and the 1.6 is from assuming MVK and macr are 1.6 times better detected than isoprene (Warneke et al., 2003). S_0 is the reagent ion signal ($S_{H3O^+} + S_{H3O^+.H2O}/1.4$; the factor 1.4 here is the relative transmission factor determined for the 38 u relative to 21 u, and isotopic factors of 667 and 500 were applied to S_{38u} and S_{21u} , resp., to get the water proton signals. The average production rate of OH due to HONO photolysis is balanced by its loss to isoprene:

$$\frac{d[OH]}{dt} = k_{phot.}^I[HONO] - k_{OH+isop.}[OH][isop.]$$

Applying steady-state and: $k_{phot.}^I[HONO] = k_{OH+isop.}[OH]_{s.s}[isop.] \quad (\text{eq5.3})$

and combining eqns. 5.1, 5.2 and 5.3, an expression for the quantity $k_{phot.}^I[HONO]$ is obtained.

$$k_{phot.}^I[HONO] = \frac{\Delta([MVK]+[macr])}{0.7\tau_{res}} = \frac{1}{0.7\tau_{res}} \frac{\Delta S_{71u}}{1.6S_{isop.}(S_0/1MHz)} 2.4 \times 10^{10}$$

Using a value of 15 ppmv for HONO in the source flow ($Q_4 = 4.4$ sccm) there is 22.8 ppbv HONO, and we get a value of $7.2 \times 10^{-4} \text{ s}^{-1}$ for the average photolysis rate of HONO. We ran the experiment again at a total flow rate of 1.45 sLpm (1/2 of normal) and the signals are shown in the right hand plot of Fig. S5.2. The residence time and the [HONO] double and with $\Delta S_{71u} = 13.3$ kHz, a value for $k_{phot.}^I$ of $8.6 \times 10^{-4} \text{ s}^{-1}$ is obtained.

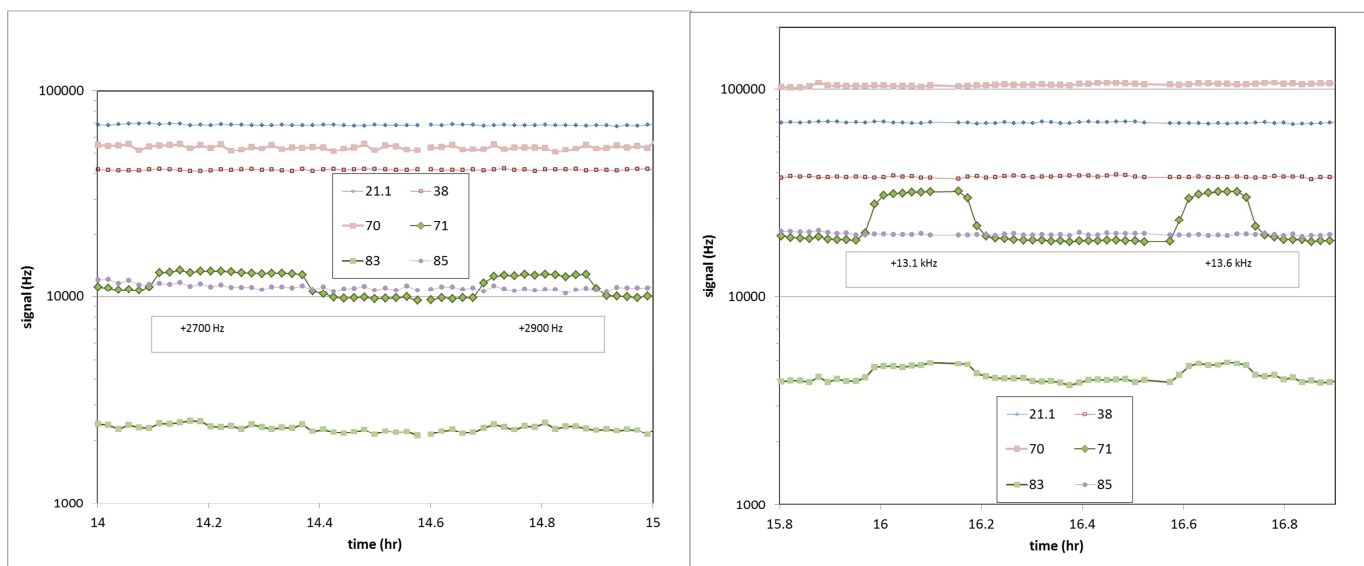


Fig. S5.2. Signals from PTRMS as a function of time. Signals at 21.1 u and 38 u are monitors for the water proton clusters, 83 u and 85 u are due to additional isoprene oxidation products. Change in signal for 71u due to turning on UV lights (on from 14.1 to 14.35 and 14.7 to 14.9) to initiate HONO photolysis are indicated in Hz. Figure on the right is with 1/2 the total flow rate whereupon [HONO], [isoprene] and the residence were doubled (UV on from 16.0 to 16.2 and 16.6 to 16.7).

S6. Ammonia conditioning and holdover.

We believe the the flow reactor wall became conditioned to ammonia when subjected to large NH_3 exposures: particle counts rose with time and there was occasionally large holdover where residual ammonia affected results for up to several days. This is shown in Fig. S6, a plot of N_p vs. date on runs surrounding (red squares depict no base added runs) days when runs with 2000 pptv NH_3 (blue diamonds) was added. On the two days when this amount of NH_3 was added (blue diamonds) N_p increased precipitously with time, increasing by more than an order of magnitude before NH_3 was removed.

This amount of ammonia affected experimental conditions, most likely through neutralizing of the acid that had accumulated on the wall. This conditioning is presumably due to ammonium bi-sulfate formation on the walls which will decrease the loss of NH_3 and more NH_3 is transported down the reactor where it can interact with the high SA levels found there. After each of the two additions, N_p without added NH_3 was quite high (red squares) and after the second run high N_p persisted for several days.

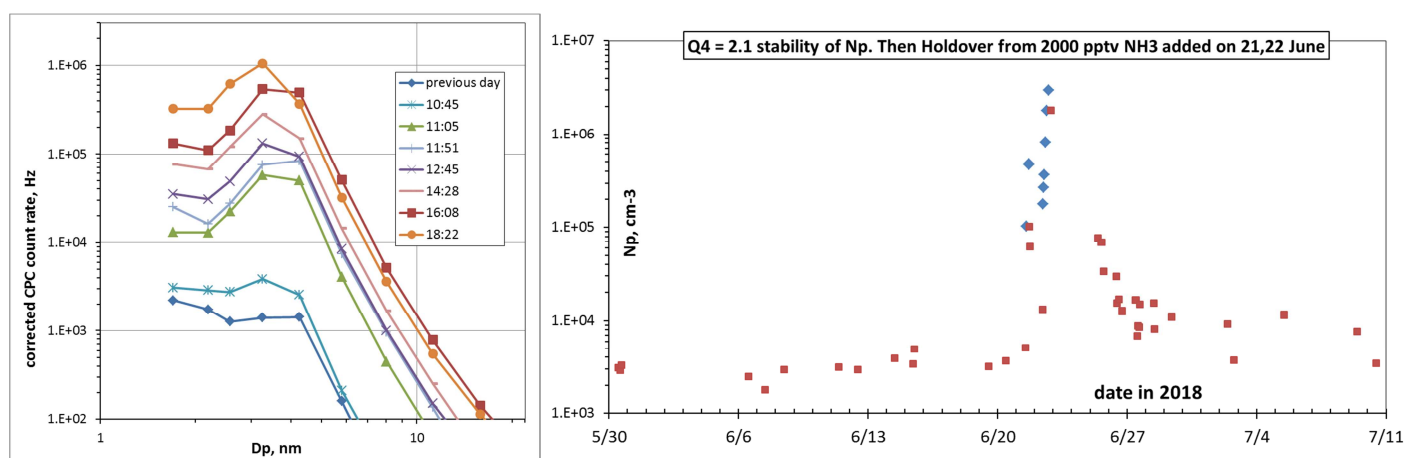


Fig. S6. Data for $Q_4=2.1$ sccm showing the effects of high exposure to ammonia. (a) Evolution of size distributions, labelled with time of day on 2018Jun22; 2000 pptv NH_3 was introduced at 10:55. (b) N_p (cm^{-3}) before and after (red squares), and during (blue diamonds), exposure of PhoFR to 2000 pptv levels of ammonia. The second set of blue diamonds are the N_p of the distributions shown in (a).

S7. Model details.

The model is a 2D representation of the flow reactor and was built upon the model presented in Hanson et al. (2017), with details of acid-base clustering presented in the Supplement of that work. In addition to changes in the flow rate (2.9 sLpm here), the present simulations included the production of H_2SO_4 from the photolysis of HONO and subsequent oxidation of SO_2 . The main inputs for the simulation are HONO and SO_2 levels, a 1st-order photolysis rate coefficient for HONO and the amount of base in the inlet. The photo-oxidation scheme and rate coefficients are shown in Table S1. The flow rate was varied in the model from 2.8 to 3.0 and the large clusters (i.e., N_p) were insensitive to flow rate. The number of acid molecules in the largest clusters in the simulation was varied from 6, 8, and 10, maintaining a maximum NH_3 -content of 3, and only small variations were observed in the concentration of the largest clusters (summing over base content). This was much in line with what we reported previously (Panta et al. 2012, Hanson et al. 2017). Presented in S1.3 above were runs where clusters were allowed to grow to 250 sulfuric acid molecules. In this work, base was introduced into

simulated 2D flow reactor uniformly distributed across the radius of the flow reactor. Section S7.1 below discusses how well this mimics the mixing of the base in the experiment.

Table S1. Photochemistry included in the simulation leading to the production of H₂SO₄. O₂ and H₂O are present in great abundance and were not simulated along with other transient species (O, HOSO₂, SO₃, HO₂SO₂.)

rxn no.	reactants			products		nomenclature and rate coefficient	unit or note
1	HONO	+	hν	→	OH + NO	$k_{\text{phot.}} = 8e-4 \text{ s}^{-1}$	s ⁻¹
2	OH	+	SO ₂	→	HOSO ₂	$k_{1x5} = 0.89e-12$	cm ³ /s
2'	O ₂	+	HOSO ₂	→	SO ₃ + HO ₂	<i>prompt</i>	a
2''	SO ₃	+	2 H ₂ O	→	H ₂ SO ₄ + H ₂ O	<i>prompt</i>	a
5a	OH	+	OH	→	H ₂ O + O	$k_{1x1wo} = 1.4e-12$	cm ³ /s
5b				→	H ₂ O ₂	$k_{1x1m} = 6e-12$	cm ³ /s
6	OH	+	HO ₂	→	H ₂ O + O ₂	$k_{1x3} = 1.1e-10$	cm ³ /s
7	OH	+	HONO	→	H ₂ O + NO ₂	$k_{1x7} = 6e-12$	cm ³ /s
8	OH	+	NO	→	HONO	$k_{1x2} = 1e-11$	cm ³ /s
9	OH	+	NO ₂	→	HONO ₂	$k_{1x6a} = 1e-11$	cm ³ /s
9b	OH	+	NO ₂	→	HOONO	$k_{1x6b} = 1.4e-12$	cm ³ /s
9b_r			HOONO	→	OH + NO ₂	$k_{_10} = 0.7$	s ⁻¹
10	HO ₂	+	NO	→	HO + NO ₂	$k_{2x3} = 8.5e-12$	cm ³ /s
11	HO ₂	+	NO ₂	→	HO ₂ NO ₂	$k_{3x6} = 1.7e-12$	
11_r			HO ₂ NO ₂	→	HO ₂ + NO ₂	$k_{_4} = 0.11$	s ⁻¹
12	HO ₂	+	HO ₂	→	H ₂ O ₂ + O ₂	$k_{3x3} = 4.8e-12$	b
13	HO ₂	+	SO ₂	→	HO ₂ SO ₂	$k_{3x5} = 3e-17$	cm ³ /s
14	{H ₂ O}	+	HO ₂ SO ₂	→	H ₂ SO ₄ + {OH}	<i>prompt</i>	c

All rates from IUPAC (Atkinson et al. 2004.) or NASA-15 except rxn. 13, the upper limit of Burrows et al. (1979). Species designations: 1, OH; 2, NO; 3, HO₂; 4:HO₂NO₂; 5: SO₂; 6: NO₂; 7: HONO; 8: HNO₃; 9: H₂O₂; 10: HOONO. a: Assumed to be very fast. b: Includes water chaperone effect. c: Speculative rate and products: OH assumed to be produced.

S7.1 Inhomogeneous base concentrations

There is a concern that base in the sidearm flow does not mix into the main flow rapidly enough to match the assumptions in the simulations. For example, base is present in this sidearm flow at a level of about 100 times the value it would be when fully mixed. In our previous work using 3D CFD models of flow reactors with similar base introduction methods (Fig. A11 in Panta et al. 2012; Figure 4 in Hanson et al. 2017), we showed that base diffusion into the sulfuric acid-laden carrier gas was rapid enough that significant cluster formation did not occur until large gradients in [base] were reduced. Appreciable cluster formation began only after base had been dispersed such that [base] was less than 10 % of its initial sidearm concentration. Cluster formation was not immediate even though the highest levels of sulfuric acid were at the top of the flow reactors where the highest levels of base were. A 2D model cannot simulate this sidearm addition of base and a workaround was presented (Hanson et al., 2017) where base was added at four times the desired level but only in the middle 1/4 of the flow, a so-called middle-fake base addition.

Shown in the figure below are results from the middle-fake simulations compared to base fully-mixed at the flow reactor inlet. More ammonia makes it down the reactor due to less interaction with the reactor wall than when ammonia is fully mixed (Fig S7.1 right: compare MidFake 40 cm to Normal 40 cm). The effect on the number of particles was an increase of about 40 % when the middle fake was used (Fig. S7.1 left). This is likely due to the increased ammonia levels downstream (compare the 40 cm radial distributions.) This is a significant effect but it is certainly within the scatter of the base-added experiments. It is likely that the effect on N_p is not large because the base is able to diffuse and establish the radial profile determined by loss on the wall before sulfuric acid builds (see Fig. S3.1.2) and significant cluster formation has commenced.

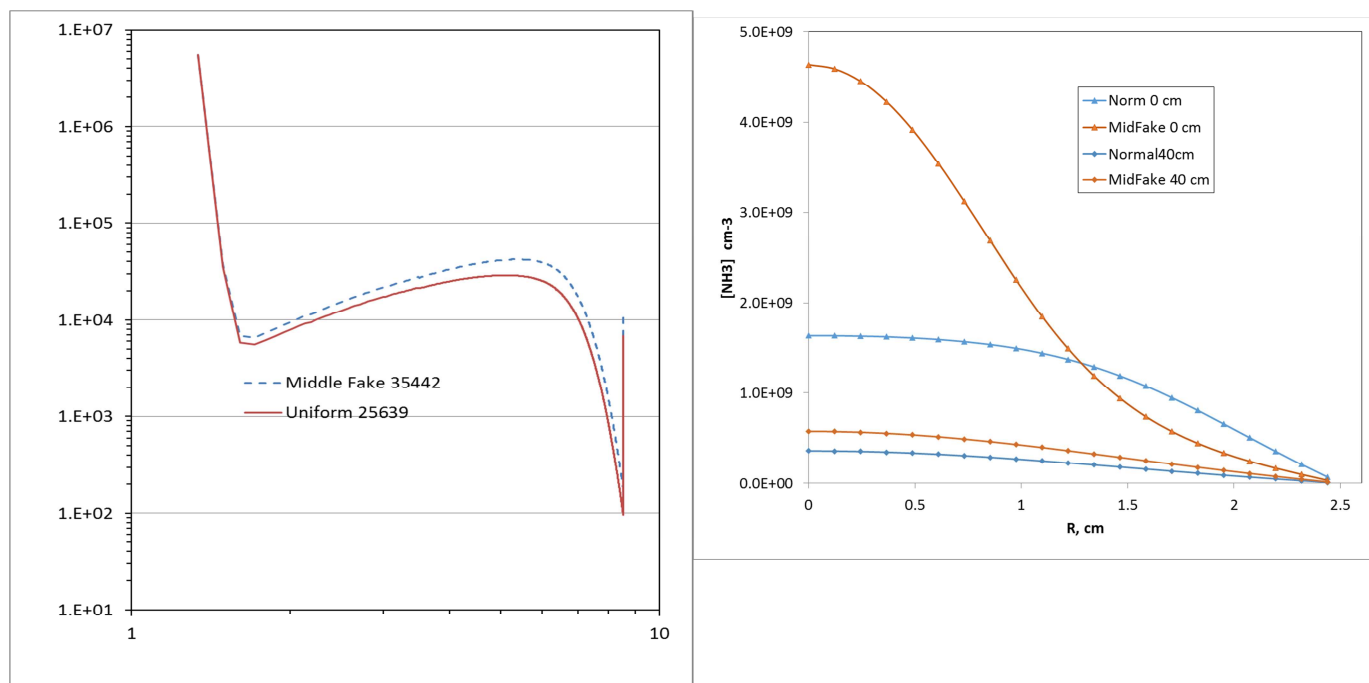
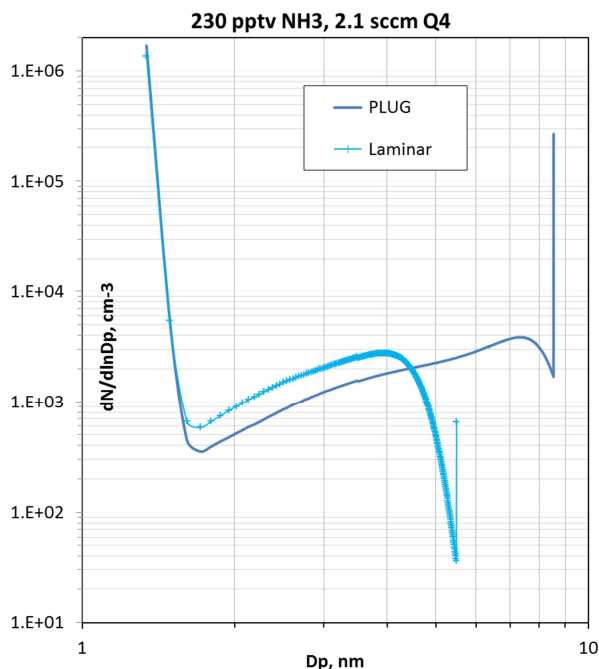


Fig. S7.1. Simulations showing the effect on size distributions (left, $dN/d\log D$ vs. D_p) and ammonia radial distribution (right) due to increasing ammonia by 300 % but confining it to the middle 1/4 (mass flow basis) of the flow reactor. *B52* thermodynamics, which is very close to NH_3_{52} thermo., was used for these simulations with 70 pptv ammonia.*

S7.2 Flow considerations

The model assumes either a fully-developed laminar or plug flow profile for the entire length of the flow reactor. With a Reynold's number of about 90 and an entrance length of ~ 14 cm (0.03 times the diameter times the Reynold's number, Goldstein, 1965 p299), it is expected that experimental conditions are best represented in the simulations using laminar flow than plug flow. This is corroborated by comparing simulations to experimental. Shown in Fig. S7.2 are simulated size distributions for laminar and plug flow for $Q_4=2.1$ sccm and 230 pptv NH_3 where the experimental mode diameter with ammonia added is about 4 nm (Fig. S1.3.1). The shape and peak of the size distribution for laminar flow agrees best with experiment as the plug flow simulation shows a leading edge mode with an ~ 8 nm diameter. Note that there is an increase in simulated N_p of about 70 % when plug flow was used compared to laminar flow. The results of these simulations reveal that the assumed flow profile does matter, particularly in the shape and peak of the size distribution.

Nonetheless, the flow at the top of the reactor may not be fully-developed laminar for some length. Since base is added in this section there may be a sensitivity to conditions that would be difficult to explore with the two-dimensional simulation. Yet sulfuric acid levels are lowest at the top of PhoFR and the effect of non-laminar



flow is probably a secondary issue more related to variability than to a systematic bias, such as a contamination problem as depicted for the high ammonia experiments (Fig. S6) and intermittent dust contamination (Fig 2a).

Fig. S7.2. Simulated size distributions for laminar flow vs. plug flow. The maximum cluster size of 1000 H_2SO_4 molecules was just big enough to capture the peak of the leading edge mode for the plug flow simulation. Although there is a spike in its abundance, the 1000-SA cluster concentration contributes only about 3% to the total number density of particles.

S8. $\text{NH}_3\text{-H}_2\text{SO}_4$ Cluster thermodynamics at 52% RH.

A set of thermodynamics for ammonia sulfuric acid clusters that merges with the free energies of the no-base clusters for 52 % relative humidity were developed here. The cluster free energies were manually set by running simulations and checking them against the experimental data for $Q_4 = 4.2$ sccm with ammonia at 500 pptv and higher. This assumes that the effect of contaminants is negligible for these conditions. Any synergistic effects are also assumed to be negligible. Because of these assumptions, the free energies must be put on a phenomenological footing.

Previously, a set of thermodynamics for ammonia- and dimethylamine-sulfuric acid clusters were determined (Hanson et al., 2017) by comparing 3D simulations to the Glasoe et al. (2015) experimental data. These thermodynamics included the base-free clusters which were taken from the phenomenological thermodynamics developed in Panta et al. (2012) for 16 % relative humidity even though the Glasoe et al. data was taken at a relative humidity of 27%. This shortcut had little impact on the acid-base thermodynamics because the experimental data was completely dominated by the presence of base molecules.

Since the majority of the data here is for a relative humidity of 52 %, a new set of binary thermodynamics was developed using the procedure used by Panta et al. (2012, see their Supporting Information, S2): anchor the H_2SO_4 dimer and trimer thermodynamics to the experimental values of Hanson and Lovejoy (2006), and for a large cluster, here the hexadecamer, set its free energy change for adding an acid to the bulk value (Wexler and Clegg, 2002). Then smoothly transition the thermodynamics between these values. Also, a given H_2SO_4 -content species is larger at 52 % RH than it is at 16 % RH and therefore the diffusion coefficients and collision rate coefficients are also affected. These new values along with the 16 % RH values of Panta et al. (2012) are listed in Table S2. Since this is a somewhat arbitrary procedure, it should be considered as exploratory.

The phenomenological ammonia-sulfuric acid thermodynamics developed here were based on the Ortega et al. (2012) thermodynamics (extended to larger clusters: NH3_I scheme of Hanson et al. (2017)) and adjusting for the 52 % RH binary system thermodynamics. Cluster free energy changes for addition of sulfuric acid were increased regularly and uniformly as ammonia molecules were incorporated into each cluster. We kept the appearance of local minimums in H₂SO₄-loss rates from a₂b₁ and a₂b₂ in accord with the NH3_I thermodynamics of Hanson et al. (2017) which followed closely the quantum chemical calculations of Ortega et al. (2012). These cluster free energies labeled NH3_52 were extended up to a₁₀b₁₀ clusters and are presented in Table S3. The largest differences from NH3_I, i.e., $\Delta G(\text{NH3_I}) - \Delta G(\text{NH3_52})$, are: more stable a₄₋₈b₀ clusters (3 to 14 kcal/mol), more stable a₆₋₈b_{1,2} clusters (2.7 to 10.5 kcal/mol), and less stable a₃₋₅b_{3,4} clusters (-8.5 to -3.5 kcal/mol). A large effect on cluster abundances was noted when selecting the free energy of a₁b₁: a factor of x3 / divide by 3 in N_p occurred when a₁b₁ was adjusted by 0.5 kcal/mol, down and up, respectively. The free energy for a₁b₁ in NH3_52 was set to -7.2 kcal/mol, 0.8 kcal/mol less stable than in NH3_I.

Table S2. Binary system free energy changes, diffusion coefficients, and forward rate coefficients. 296 K Values for 16 and 52 % RH are shown.

<i>n</i>	16 % RH, 60 wt. % H ₂ SO ₄				52 % RH, 42 wt. % H ₂ SO ₄			
	ΔG^0 ^a kcal/mol	D _p ^b nm	D _c ^c cm ² /s	k _{for} (10 ⁻¹⁰ cm ³ s ⁻¹) ^d	ΔG^0 ^a kcal/mol	D _p ^b nm	D _c ^{c,e} cm ² /s	k _{for} (10 ⁻¹⁰ cm ³ s ⁻¹) ^d
1		0.69	0.0806			0.82	0.0760	
2	-6.5	0.87	0.0582	4.25	-6.6	1.04	0.0480	4.95
3	-8.3	0.99	0.0445	4.70	-8.8	1.19	0.0379	5.47
4	-9.9	1.09	0.0367	5.17	-10.6	1.31	0.0319	6.02
5	-11.4	1.18	0.0316	5.62	-12.2	1.41	0.0278	6.55
6	-12.8	1.25	0.0280	6.04	-13.7	1.50	0.0249	7.03
7	-14.2	1.32	0.0253	6.43	-15.0	1.58	0.0227	7.49
8	-15.5	1.38	0.0231	6.80	-16.2	1.65	0.0209	7.93
9	-16.4	1.43	0.0214	7.16	-17.2	1.71	0.0195	8.34
10	-17.0	1.49	0.0199	7.50	-18.1	1.77	0.0183	8.74
11	-17.3	1.53	0.0187	7.83	-18.8	1.83	0.0173	9.12
12	-17.5	1.58	0.0177	8.14	-19.4	1.88	0.0164	9.49
13	-17.6	1.62	0.0167	8.45	-19.9	1.94	0.0156	9.84
14	-17.6	1.66	0.0159	8.74	-20.3	1.98	0.0149	10.2
15	-17.6	1.70	0.0152	9.03	-20.6	2.03	0.0143	10.5
16					-20.8	2.07	0.0138	10.8
17					-20.9	2.117	0.0133	11.2
18					-21.0	2.157	0.0128	11.5
19					-21.1	2.197	0.0124	11.8

^a Based on scheme E of Panta et al. (2012) without the T² dependence which was needed for their non-isothermal simulations. ^b D_p is mass diameter and fixed densities and bulk compositions are assumed: 1.50 and 1.32 g/cm³ for 60 and 42 wt. % H₂SO₄ at 16 and 52 % RH, respectively. ^c In 1 atm N₂. Humidity dependent monomer diffusion coefficient from Hanson and Eisele (2000) with an assumed T^{1.75} dependency. ^d Rate coefficient (McMurry, 1980) to form *n*th cluster, from monomer plus (*n*-1)th cluster. ^e For *n*=3 and larger, D_c = 0.0737n^{-0.605} fits well the diffusion coefficients (Lennard-Jones approach) of Mason and Monchick (1962) using the ϵ/k parameter of water (509 K) for the H₂SO₄-H₂O clusters. Values are also within 10 % of the hard-sphere diffusion coefficients of Wilke and Lee (1955).

Table S3 Scheme NH3_52 standard free energies at 298 K of $a_i b_j$, kcal/mol. Values of i across the top, j down the left side.

	# of acids in the cluster										
	0	1	2	3	4	5	6	7	8	9	10
0	0	0	-6.6	-15.4	-26	-38.2	-51.9	-66.9	-83.1	-100.3	-118.4
1	0	-7.2	-20.5	-31.2	-43	-56	-70.3	-85.8	-102.5	-120.1	-138.7
2	4	-11.3	-30.5	-45	-59	-73	-88	-104.2	-121.4	-139.5	-158.5
3	8	-14	-36	-55.5	-72	-87.6	-103.5	-120.3	-138.2	-157	-176.8
4	9.5	-15.5	-39.8	-63	-83	-100	-117	-134.8	-153.7	-173.6	-194.5
5	10.7	-16.5	-42.5	-67.3	-90.3	-110.5	-129.3	-148.5	-168.5	-189.5	-211.5
6	11.9	-17.5	-45.2	-72	-96.5	-118.5	-139.5	-160	-181	-203	-226
7	13	-18.5	-47.3	-76.5	-102	-125.5	-148	-170	-192.5	-216	-240.5
8	13.5	-19.4	-49.5	-80.5	-108	-132.5	-156	-179.5	-203	-227.5	-253
9	14	-20.3	-51.5	-84	-113.5	-139	-163	-187	-211	-236	-262
10	14	-21	-53.5	-87.5	-118	-144.3	-169	-193.7	-218.5	-244	-270.5

S9. Effect of SO₂.

Simulated H₂SO₄ profiles are sensitive to the value of this rate coefficient. Using low values yields smaller dependencies on SO₂ for N_p and size: a value of 1×10^{-17} cm³/s had N_p increase by about 50 % as Q₁ was increased from 8 to 50 sccm while a rate coefficient of 1×10^{-18} cm³/s had a 22 % increase. Increasing this rate coefficient to 1×10^{-16} cm³/s had large effects: as Q₁ varied from 8 to 50 sccm, particle size roughly doubled and N_p increased by an order of magnitude. A value of the order of 10^{-16} cm³/s along with generation of OH in the reaction is probably the limit for simulations to remain congruent with the data. On the other hand, if a wall loss for HO₂ is significant in the experiment, much larger values for the rate coefficient would be needed in the simulations for the reaction to have significant effects.

Alternative explanations for an SO₂ dependence include uncertainties in HONO concentrations as well other clustering reactions. More HONO in the flow exiting the source (and a smaller first-order photolysis rate to compensate) would cause predicted N_p to have an increased dependence on SO₂. SO₂ may react with oxidants within the small particles, leading to their growth.

The dependencies upon SO₂ were much smaller when minute amounts of dimethylamine were included in the model. Low levels of (0.005 pptv) dimethylamine gave simulated N_p in the 10^4 cm⁻³ range but at this level its ability to influence the change in N_p with H₂SO₄ was limited due to the amine being scavenged by clusters. This suggests that a potential contaminant in our system is not a strong nucleator like dimethylamine.

Atkinson, R., D. L. Baulch, R. A. Cox, J. N. Crowley, R. F. Hampson, R. G. Hynes, M. E. Jenkin, M. J. Rossi, and J. Troe, Evaluated kinetic and photochemical data for atmospheric chemistry (IUPAC): Volume I - gas phase reactions of Ox, HOx, NOx and SOx species *Atmos. Chem. Phys.*, **4**, 1461-1738, <https://doi.org/10.5194/acp-4-1461-2004>, 2004.

NASA-15: Chemical Kinetics and Photochemical Data for Use in Atmospheric Studies, JPL Publication No. 15-10, https://jpldataeval.jpl.nasa.gov/pdf/JPL_Publication_15-10.pdf.

Hanson, D. R.; Eisele, F. L., Diffusion of H₂SO₄ in Humidified Nitrogen: Hydrated H₂SO₄, *J. Phys. Chem. A*, **2000**, *104*, 1715–1719.

Hanson, D. R.; Lovejoy, E. R., Measurement of the Thermodynamics of the Hydrated Dimer and Trimer of Sulfuric Acid, *J. Phys. Chem. A*, **2006**, *110*, 9525–9528, doi:10.1021/jp062844w.

Hanson, D. R., Koppes, M., Stoffers, A., Harsdorf, R., and Edelen, K., Proton transfer mass spectrometry at 11hPa with a circular glow discharge: Sensitivities and applications, *Int. J. Mass Spectrom.*, **282**, 28–37, doi:10.1016/j.ijms.2009.01.021, 2009.

Liu, Y. J., Herdinger-Blatt, I., McKinney, K. A., and Martin, S. T.: Production of methyl vinyl ketone and methacrolein via the hydroperoxyl pathway of isoprene oxidation, *Atmos. Chem. Phys.*, **13**, 5715-5730, <https://doi.org/10.5194/acp-13-5715-2013>, 2013.

Wennberg et al., Gas-Phase Reactions of Isoprene and Its Major Oxidation Products, *Chem. Rev.* **2018**, *118*, 3337–3390, DOI: 10.1021/acs.chemrev.7b00439

Warneke, C., J. A. de Gouw, W. C. Kuster, P. D. Goldan, and R. Fall, Validation of atmospheric VOC measurements by proton-transfer-reaction mass spectrometry using a gas-chromatographic pre-separation method, *Environ. Sci. Technol.*, **37**, 2494, 2003.

McMurry, P. H. Photochemical Aerosol Formation from Sulfur Dioxide: A Theoretical Analysis of Smog Chamber Data. *J. Colloid Interface Sci.* **1980**, *78*, 513-527.

Monchick, L.; Mason, E. A. The Transport Properties of Polar Gases. *J. Chem. Phys.* **1961**, *35*, 1676.

Mason, E. A.; Monchick, L. Transport Properties of Polar-Gas Mixtures. *J. Chem. Phys.* **1962**, *36*, 2746.

Wilke, C. R. and C. Y. Lee, Estimation of Diffusion Coefficients for Gases and Vapors, *Ind. Eng. Chem.*, **1955**, *476*, 1253-1257 <https://doi.org/10.1021/ie50546a056>

Syomin, D. and B. J. Finlayson-Pitts, HONO Decomposition on Borosilicate Glass Surfaces: Implications for Environmental Chamber Studies and Field Experiments, *Phys. Chem. Chem. Phys.* **5** 5236 (2003)

Goldstein, S. ed. "Modern Developments in Fluid Dynamics", New York, Dover Publications, 1965.